Analyzing Simulated Martian Weather Data

Brian Ward   Mentors: Leslie K. Tamppari, Nathaniel J. Livesey

NASA Jet Propulsion Laboratory, California Institute of Technology   **CL#20-3943**

Abstract

In order to study the ability of a proposed submillimeter limb sounder to study Mars' atmosphere, we simulate its theoretical performance. Software was created to enable comparisons of output from a Martian Global Climate Model, taken to be "truth", to a set of simulated observations of that model output. The comparisons were based on a variety of metrics including several which have been previously studied, as well as ones which would be unique to this new instrument's capabilities. Through this analysis, we are able to understand the usefulness and limitations of such an instrument, which performs well enough to distinguish between current models. This also lays the groundwork for further optimizing studies to determine the exact configurations and orbits which would be best suited to answer the posed scientific questions.

Contents

1. Overview

Understanding weather on Mars is essential for the continued safe exploration of the planet. While much is known about the macro-scale weather patterns on Mars, very little has been directly measured of the Martian wind conditions. Similarly, little is known about the water vapor distribution and transport within the Martian atmosphere. In hopes of improving the data collection in these important areas, which would in turn allow for better input constraints to be put on Mars climate models, new measurement techniques and instruments are required.

The primary objective of this summer was to continue the examination of the techniques and instrument proposed in [Read et al., 2018], specifically the use of a submillimeter limb sounder similar to those employed in atmospheric observations of Earth to gain these necessary insights into the Martian atmosphere. By studying simulated measurements of fields extracted from the output of the *Laboratoire de Météorologie Dynamique* [LMD] Mars Global Climate Model [GCM], we were able to verify if the proposed instrument could answer the inquiries about water vapor distribution and

wind fields. This is a continuation of the work done in [Banfield et al., 2019].

To that end, the main work of the summer consisted of the creation of software tools to aid in the loading and analysis of datasets representing the atmospheric state on Mars. The first such dataset was the output of the LMD Mars GCM provided by François Forget. This consisted of approximately one Mars year of atmospheric water vapor, wind, and temperature data across the entire planet. This dataset was then used as the basis for extracting samples along an orbit for a potential spacecraft. A 300km-altitude sun-synchronous (92° inclined) orbit was selected for the simulation. This second dataset consisted of profiles measured every 75 seconds along the orbit for the same Mars year, with representative noise added to simulate data retrieved from a real spacecraft.

The simulated instrument views the atmosphere with two separate independently steerable telescopes, one is chosen to always view the atmosphere in a meridional (North-South) direction, the other always views zonally (East-West), enabling the measurement of "vector" (i.e., 2D) winds. In this configuration, the latitudinal spacing of the East-West views increases significantly in the polar regions (a consequence of the interaction between the orbital and viewing geometry), leading to "gaps" in some of the figures to be shown later in this report. Future work will examine other viewing strategies that avoid this undesirable property of the sampling.

This study is focused on the abundance of atmospheric water vapor. The simplest view of this is total atmospheric water over time (e.g. [Smith, 2002] Fig. 8), allowing comparisons of broad global trends between the model output and our simulated instrument. We also studied water va-
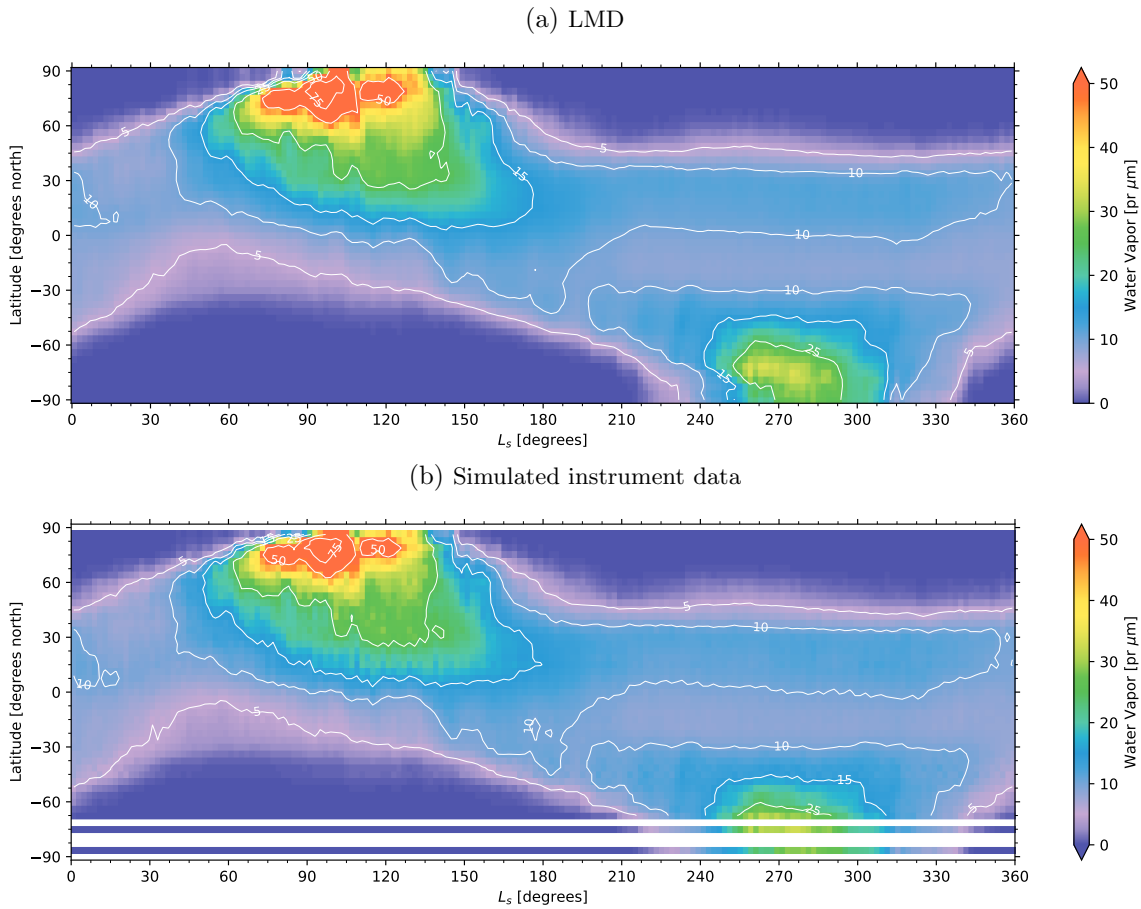
(a) LMD

(b) Simulated instrument data

Fig. 1: Zonal average water vapor column abundances as a function of latitude and L_s.

por column abundances as a function of time and latitude (e.g. [Smith, 2002] Fig. 5) to understand the relative location of atmospheric water throughout the Mars year, and water vapor column abundances as a function of latitude and longitude (e.g. [Smith, 2002] Fig. 10) to understand the variations in spatial distributions of water vapor during the annual cycle. We additionally looked at views of water vapor mixing ratios as a function of latitude and altitude in order to see individual snapshots in time. We have also laid the basis for future work in analyzing water vapor meridional transport (e.g. [Steele et al., 2014] Fig. 13 and [Haberle et al., 2019] Fig. 4.2) in order to understand the movement of water vapor at various times of year, but that work is only just beginning.

To facilitate the generation of these figures and also allow direct comparisons, the simulated instrument data had to be transformed into a similar format as the GCM output. This required placing the data into bins based on its place in latitude, longitude, and time. Once completed, we had recreated the kind of fully processed instrument output one might expect from an actual spacecraft, with the added benefit of also having the "truth" (LMD output) that data were retrieved from. These data processing functions were also generalized

to allow further exploration in future studies.

2. Results

2.1 Annual Water Cycle

Figure 1 above displays column water vapor abundances as a function of latitude and season (in solar longitude [L_s]) for both the LMD output data and the data from the simulated instrument, both to the same coarseness in latitude and L_s (See Methods for specifics on the grid used).

The LMD data (top panel) shows the highest abundances between $L_s = 90°$ and $L_s = 120°$ in the northern polar region, with another smaller peak during south pole spring (around $L_s = 270°$). Large dry areas dominate the south and north pole during their respective winters. These match up well with existing data from real Martian observations, such as those retrieved from the Thermal Emissions Spectrometer [TES] or Mars Atmospheric Water Detectors [MAWD] [Smith, 2002].

These same dominating trends are visible in the simulated instrument data (bottom panel) as well, though with some
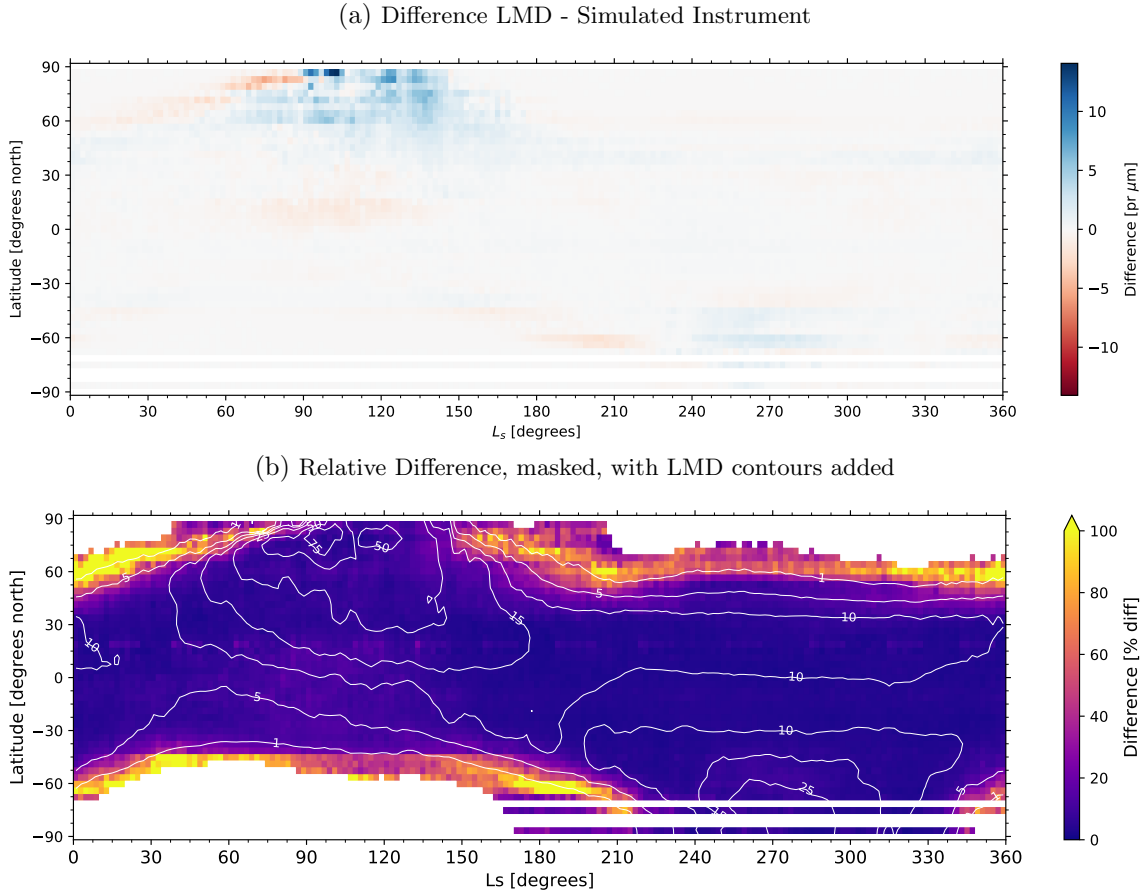
(a) Difference LMD - Simulated Instrument

(b) Relative Difference, masked, with LMD contours added

Fig. 2: The difference between the LMD output column abundances and the simulated instrument. Top: The exact difference, LMD - Simulated instrument. Bottom: The relative difference between the two, with points where the LMD abundance was < 0.05 pr-μm removed. This plot has the abundance contours from LMD applied to show areas of interest.

distinct differences. Several latitude bands south of $-60°$ are missing, due to the orbital sampling issues discussed in Section 1. This makes characterization of the south pole summer behavior more difficult, a factor that will affect several of our subsequent analyses. The plot is also less smooth, particularly in regions that are transitioning from higher abundances to lower ones. This jaggedness is understandable considering the large amount of information lost when going from a complete global dataset to individual profiles sampled along an orbital measurement track.

To understand the behavior of the simulated instrument more precisely, it is easier to look at plots of the differences between the two datasets. Figure 2 shows the difference between the datasets (top panel, in precipitable μm) as well as the relative difference, given as a percentage of the LMD totals. The relative difference plot has had values where the LMD totals fall below 0.05 pr-μm removed to avoid placing undue emphasis on cases where the true abundance of water vapor is very low, and the measurement system could not be

reasonably expected to measure with strong signal-to-noise. Additionally, this plot has contours of the original LMD column abundances added for reference.

The differences (top) show very promising results. The mean difference is 0.15 pr-μm, the maximum positive difference is $+14$ pr-μm, and the maximum negative difference is -5 pr-μm, encouraging considering the large dynamic range of column water vapor. Additionally, the majority of the largest differences appear in the north pole region during the wet season, previously identified to be the wettest part of the annual water cycle. In general, the simulated measurements are slightly drier overall, with the majority of the difference being in the positive direction. It is once again difficult to characterize the south polar performance, but the available data are quite close to the truth output.

The relative difference (bottom) confirms that the areas of largest difference coincide with the areas of the most water. The north pole spring and the available south pole spring measurements perform similar to much of the rest of the planet
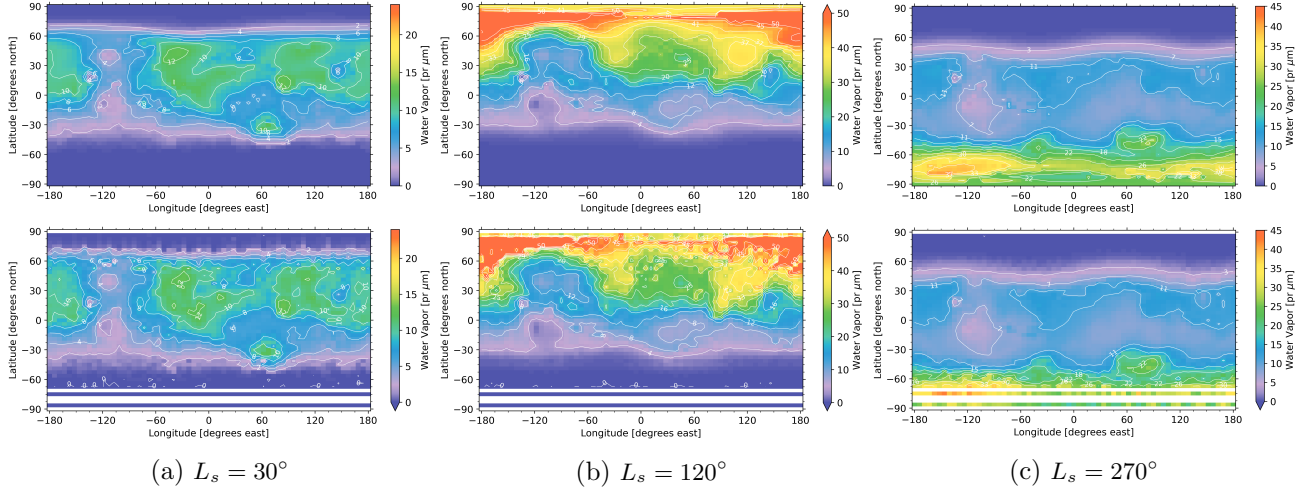
(a) $L_s = 30°$ (b) $L_s = 120°$ (c) $L_s = 270°$

Fig. 3: Spatial distribution of water vapor at three different times of year. Note the different color scale for each time period. Top: LMD output. Bottom: Simulated instrument data.
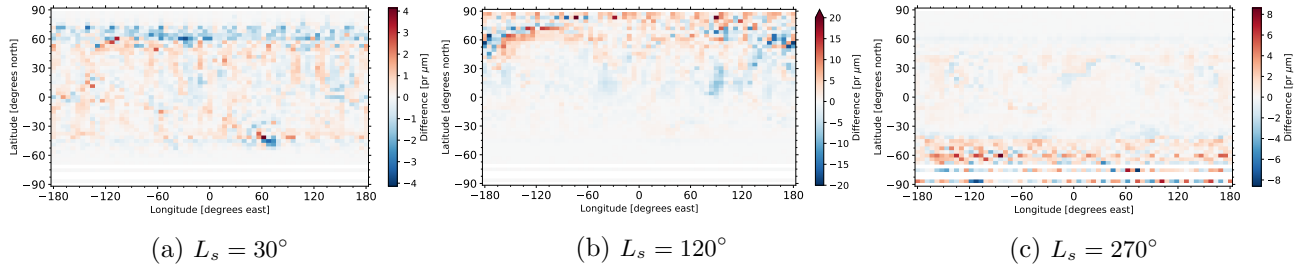

(a) $L_s = 30°$ (b) $L_s = 120°$ (c) $L_s = 270°$

Fig. 4: Differences, spatial distributions of water vapor at three different times of year. Note the different color scale for each time period.

on a percentage basis (both within 10% of LMD). This graph does show very large percentage differences in boundary regions with < 1 pr-μm of water. As these regions feature so little water, even a small difference (as shown in the top panel) amounts to a very large percentage. This is important to consider also for the regions which are not shown in the plot, which feature near-zero values for their column abundances. Outside of these regions of low total abundance, the relative difference is generally below 20%.

Both of these plots show some banding affects, most obviously near 60° north on the difference plot and between 15° and 20° north on the relative differences. This is a result of the chosen orbit and sampling method, and further studies in different orbits or instrument configurations are needed.

2.2   Spatial Distribution of Water

In order to investigate the instrument's ability to determine the spatial distribution of water, several points throughout the year were chosen for comparison. First was $L_s = 30°$, during the planet-wide dry season, followed by $L_s = 120°$, the northern hemisphere wet season, and $L_s = 270°$, the southern

hemisphere wet season. For each of these, a window of one Martian month (30° L_s) centered on the given time was used to provide complete coverage of the planet in the simulated orbit. These results are shown in Figure 3.

Much like the annual water cycle, it is immediately clear that the simulated instrument does a qualitatively good job of retrieving the desired information. The simulated observations (bottom row) aligns well to the eye with the LMD "truth" data (top), with the familiar missing latitude bands near the south pole and the more jagged lines being the main differences on first glance. The jagged lines are a function of the sampling and relatively small time window used, and they become more or less smooth if the window is increased or decreased. A window smaller than $\approx 15°$ of L_s leads to gaps where a latitude-longitude bin has no samples during the time window requested. Beyond these, the regions of high and low abundance align fairly well in each time window.

Figure 4 shows the differences between the LMD output and the simulated instrument for each time frame. Here we see noticeably different behavior in each time frame. The period around $L_s = 30°$ has the lowest differences, in the range of ± 4 pr-μm. However, there is much less water in the

atmosphere overall at this time, and the errors here are spread throughout most of the planet. $L_s = 120°$ is much more variable, with the extrema being offset by ± 20 pr-μm. In this case, the greatest differences are concentrated in the north polar region, which also features the highest abundances at >50 pr-μm. The case of $L_s = 270°$ is hardest to characterize, as we are once again unable to retrieve data in most of the polar region, but it features a more modest range of differences at ± 8 pr-μm. In general, areas of larger abundances lead to the largest differences, similar to the zonally averaged case analyzed in the previous section. On a percentage basis, this means the error is still quite low (below 15%) for regions where there is an appreciable amount of water vapor. It is important to note the $L_s = 30°$ case, as it does not feature areas of large abundances, unlike the other two time windows. This leads to smaller magnitude errors (similar on a percentage basis), but they are much more spread out across the planet rather than localized at specific areas.

This is all done without taking into consideration Mars' varied topography. It is possible to scale this kind of plot by surface pressure to smooth out the affects of topology (one such method is discussed in [Smith, 2002]), but that is not explored at this time.
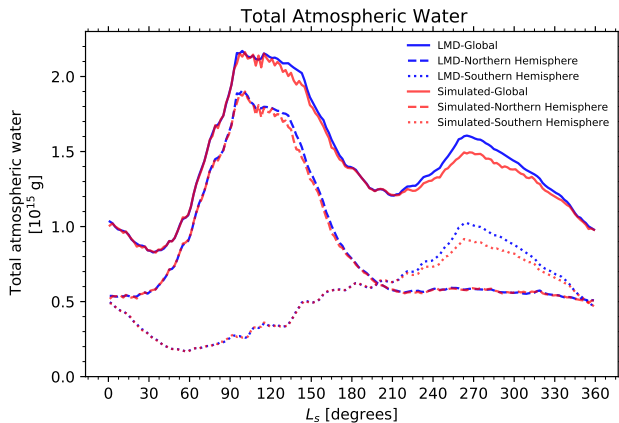
Fig. 5: The total atmospheric water by weight in each hemisphere as a function of L_s

2.3 Total Atmospheric Water

Figure 5 shows the total amount of water vapor in the atmosphere as a function of season. This shows the same annual trends mentioned earlier, with the most amount of atmospheric water around $L_s = 120°$, primarily in the northern hemisphere, with another smaller maxima around L_s 270, accounting for the south pole's spring. These trends are also broadly captured by the simulated instrument data, though it is clearly lower at several points.

Notable losses occur at the end of the northern hemisphere wet season and the peak of the southern hemisphere wet sea-

son (L_s 240° – 330°). The former is the same period as discussed in the annual water cycle discussion. This period features the most water vapor on the planet, and therefore it also features the largest magnitude discrepancies in our retrieval. The second discrepancy is likely accounted for by the missing observational data south of $-60°$, as discussed in Section 1. The overall difference is much larger in the southern hemisphere, though it is mainly apparent during the wet period.
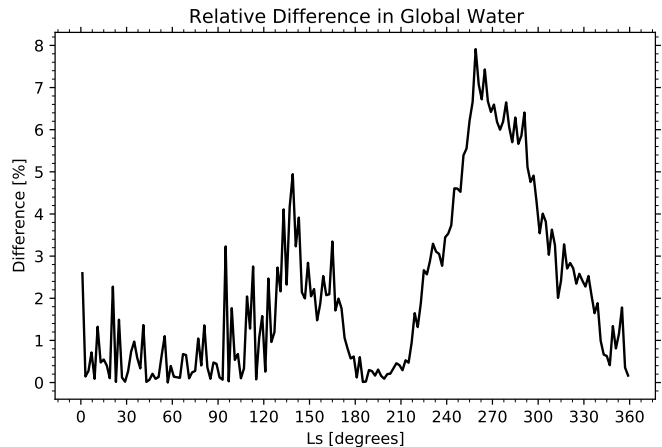
Fig. 6: The difference between the LMD and simulated data, as a percentage of the LMD total

The relative difference in global totals is shown in Figure 6. From this graph it is clear that even during the southern hemisphere wet season, the difference between the simulated retrieval and the LMD data is only 8% of the LMD water totals. More complete coverage of the southern hemisphere could lower these results to as low as 5%, the highest percent difference we see for most of the rest of the year, or lower.

The instrument is still successful in identifying the seasonal trend of water vapor abundance, as well as correctly identifying maxima and minima of that trend.

2.4 Vertical Distribution of Water

To assess the instrument's capability to observe the vertical distribution of water in the Martian atmosphere, the same L_s windows from Section 2.2 were used, as was the window size of 30°. These plots are shown in Figure 7. The vertical coordinate is provided both in pressure (which underlies our coordinate system) and approximate altitude.

The qualitative shape and distribution of the water vapor in the atmosphere is very similar between the LMD output (top) and simulated instrument (bottom) for all three time windows. The missing latitude bands once again serve as the most noticeable difference between each.

Taking an absolute difference of these, as is shown in Figure 8, shows that these are indeed quite close. While there are
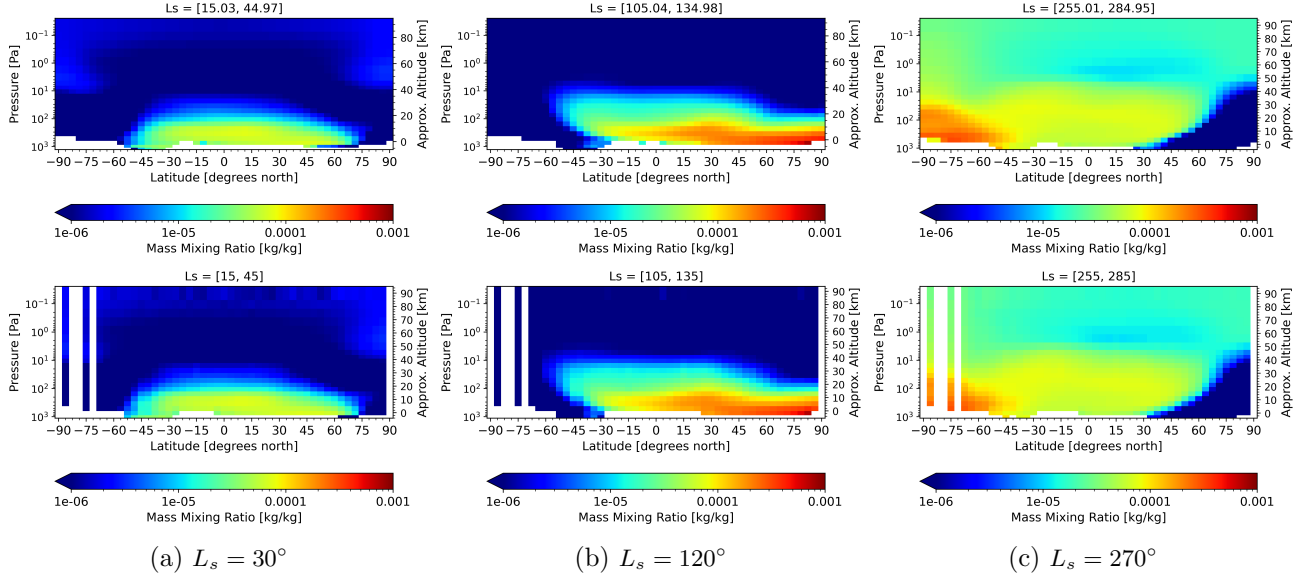
Fig. 7: Vertical distribution of water vapor at three different times of year (zonal averages), logarithmic scale. Top: LMD output. Bottom: Simulated instrument data which has been resurfaced to match the LMD pressure levels.
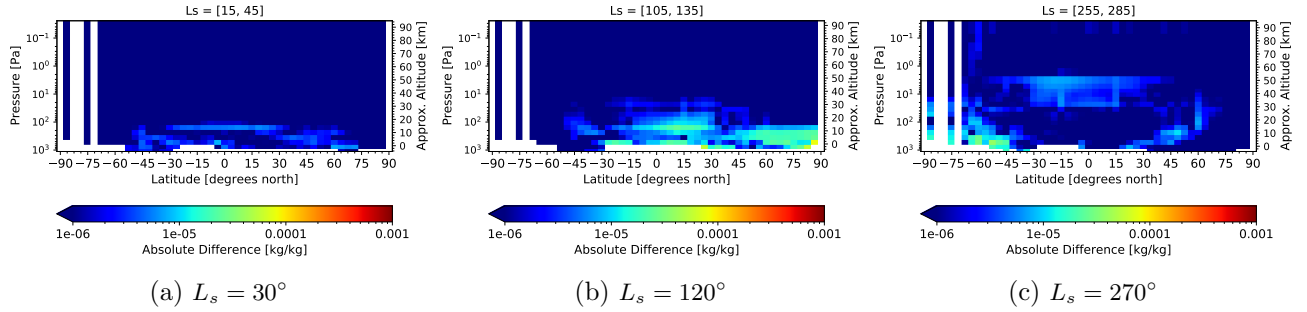

Fig. 8: Absolute differences between zonal average vertical distribution of water vapor at three different times of year, log scale.

many points that differ, especially in the regions of the original plots with the most water vapor, these differences are at least an order of magnitude smaller than the data itself. Similar to the spatial distribution plots, the dry season ($L_s = 30°$) case has the smallest absolute differences, but the relatively lower amounts of total water during this period actually mean it performs worse than the cases with more water.

3. Conclusion

After studying the performance of the simulated sub-mm instrument, we can conclude that proposed instrument can report on the studied figures to a useful degree of accuracy. This would not only allow the further refining of models, but can also answer questions that have not previously been possible to address about the vertical distribution of water vapor. Further studies could confirm if additional new questions may be

answered by such an instrument, specifically studies of wind and water vapor transport in the Martian atmosphere.

The simulated instrument data often led to results within 10% of the LMD "truth" data, though this obviously depends on the metric in question. The errors found are all sufficiently small that differentiation between existing climate models would be possible. Further studies may use different GCM output as the "truth" data to study the extent of this possibility in full. Furthermore, many of the most noticeable errors are a direct result of the sampling strategy, including but not limited to the missing latitude bands south of $-60°$.

Many possible improvements could be studied to remedy this issue. The 75 second limb scan interval could be shortened. This would reduce the size of gaps and increase the amount of data collected overall, at the cost of increased noise (for example, halving the length of scans would lead to approximately a $\sqrt{2}$ increase in noise). However, that increase in noise would not be a concern after averaging several profiles

together, so this is a valid option if individual atmospheric profiles are permitted to be noisier.

Further studies can also investigate if the 92°-inclined orbit is optimal or if another orbit leads to better coverage of key areas of the planet.

Finally, the instrument configuration (steering antennas, which for this study were steered to seek North and East) could be iteratively optimized to find the best compromise between coverage and usefulness.

All these improvements could only lead to even more significant results.

4. Methods

All software produced as a result of this project was coded in Python 3.7, with several important libraries added in addition. The primary library for data storage and manipulation was xarray [Hoyer and Hamman, 2017], which allows the reading and writing of the standard netCDF format. Additionally, SciPy [Virtanen et al., 2020] was used for the loading of simulation files generated in the IDL programming language, and was used for several calculations. L_s (when not provided in the datasets) was calculated using the marstime package based on [Allison, 1997] and [Allison and McEwen, 2000].

The LMD dataset was loaded as-provided by Forget, with the only addition being the L_s calculation. The data were provided in bins 3.75° latitude by 5.625° longitude over 24 pressure levels, with 12 timesteps per sol for 669 sols.

Simulated instrument data were provided in an IDL save file, which was then loaded into a netCDF file for later manipulation. These data are ≈1.2 million profiles, each representing a 75 second limb scan from one of two antennas. For this report, the configuration in which the antennae seek North and East measurements was used, as described in Section 1.

This dataset is generated in three stages. First, the data is sampled from the LMD model along the orbital track. Then, these profiles are resurfaced from the 24 LMD levels to have 65 pressure levels using log-pressure interpolation. Finally, averaging kernels were applied based on simulations of the performance of the sub-mm instrument in the Martian atmosphere, provided by William G. Read, see Fig. 9. The last two files labeled in Fig. 9 were used in this study, with figures generated using the second to last (red markings). The difference in finalized retrievals between these two retrieval profiles was less than 0.06pr-μm in any given zonal average. This final dataset is representative of the actual data retrieval, with appropriate noise.

These profiles were then grouped into bins 2° of L_s, with a latitude by longitude grid identical to the grid used in the LMD data. Direct comparisons required additional binning to be performed to align the times and pressures of the simulated data and LMD output. This may itself be a source of error in some figures due to the slight differences in time binnings, but
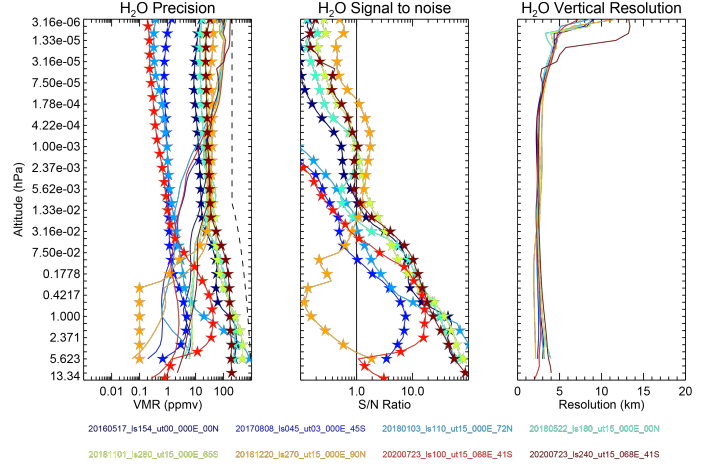

Fig. 9: Precision information generated by William G. Read, used to simulate retrievals.

neither dataset should ever differ by more than a fractional degree L_s.

Water vapor column abundances were calculated for each column using code adapted to water vapor on Mars, based on a general, Earth-based IDL routine. Data which is missing (due to being in a pressure level which is subsurface) is dropped for each column individually before the computation.

4.1 Verification with Ames Output

Additional data from the NASA Ames Research Center Mars GCM was used to help verify the calculations used for column abundances. At the moment we did not run extract simulated data for a spacecraft orbit, though that is a possible extension. Therefore, these plots were used as broad checks on the reasonability of our outputs (See Figure 10 below).

Ames data were also used as a reference for the development of tools to calculate water vapor meridional transport for future use in analyzing the proposed instrument. This was calculated using the equation

$$[\overline{Q_\phi}] = \frac{2\pi r \cos(\phi)}{g} \int_0^{P_{\mathrm{surf}}} [\overline{qv}] \, dp \qquad (1)$$

This calculation was decomposed into the constituent parts using the relation

$$[\overline{qv}] = [\bar{q}][\bar{v}] + [\bar{q}^*\bar{v}^*] + [\overline{q'v'}] \qquad (2)$$

These are based on the discussions in [Peixoto and Oort, 1992, Chapter 4, 12]. The result can be seen in Figure 11 with a comparison from [Haberle et al., 2019].
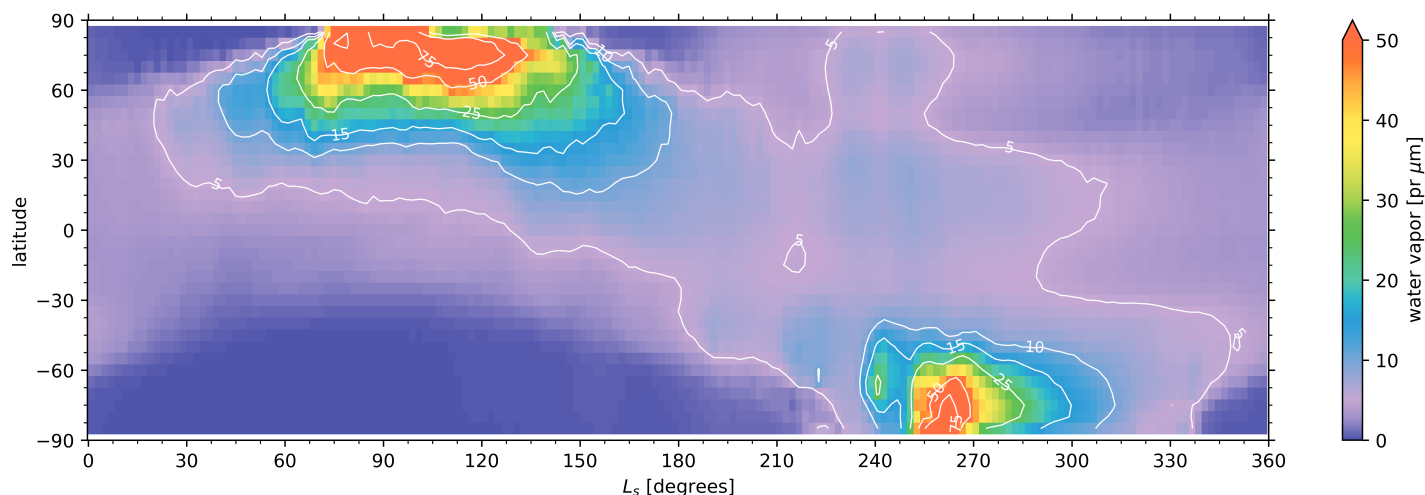
Fig. 10: Zonal average water vapor column abundances as a function of latitude and L_s calculated for the NASA/Ames GCM
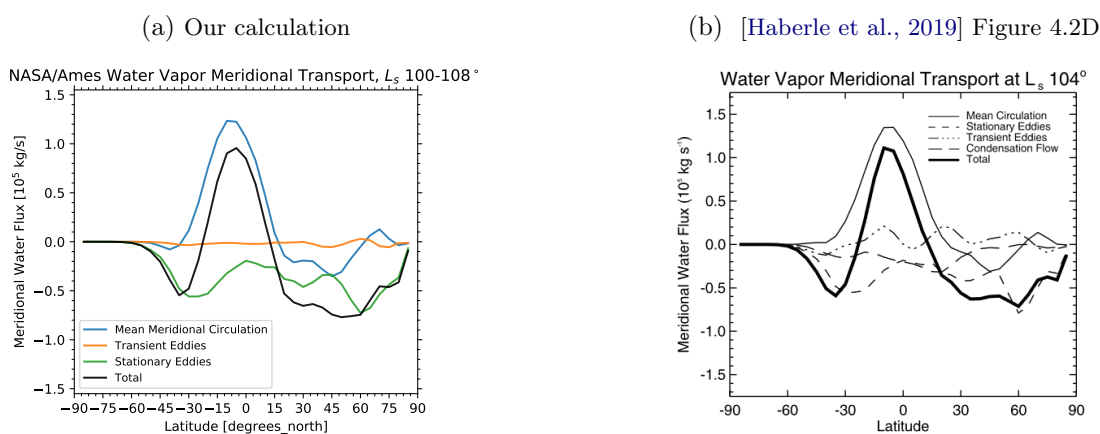
(a) Our calculation

(b) [Haberle et al., 2019] Figure 4.2D

Fig. 11: Meridional Water Vapor Transport around $L_s = 104°$ in the NASA/Ames GCM.

Acknowledgments

References

[Allison, 1997] Allison, M. (1997). Accurate analytic representations of solar time and seasons on mars with applications to the pathfinder/surveyor missions. *Geophysical Research Letters*, 24(16):1967–1970.

[Allison and McEwen, 2000] Allison, M. and McEwen, M. (2000). A post-pathfinder evaluation of areocentric solar coordinates with improved timing recipes for mars seasonal/diurnal climate studies. *Planetary and Space Science*, 48(2-3):215–235.

[Banfield et al., 2019] Banfield, D. B., Tamppari, L. K., and Livesey, N. J. (2019). Assessing observability of mars winds using various options in sub-mm limb sounding. In *EPSC-DPS2019 meeting, Centre International de Conférences de Genève (CICG)*, Geneva, Switzerland.

[Haberle et al., 2019] Haberle, R. M., Kahre, M. A., Hollingsworth, J. L., Montmessin, F., Wilson, R. J., Urata, R. A., Brecht, A. S., Wolff, M. J., Kling, A. M., and Schaeffer, J. R. (2019). Documentation of the NASA/Ames legacy mars global climate model: Simulations of the present seasonal water cycle. *Icarus*, 333:130–164. https://doi.org/10.1016/j.icarus.2019.03.026.

[Hoyer and Hamman, 2017] Hoyer, S. and Hamman, J. (2017). xarray: N-D labeled arrays and datasets in Python. *Journal of Open Research Software*, 5(1).

[Peixoto and Oort, 1992] Peixoto, J. P. and Oort, A. H. (1992). *Physics of Climate*. American Institute of Physics, New York.

[Read et al., 2018] Read, W. G., Tamppari, L. K., Livesey, N. J., Clancy, R., Forget, F., Hartogh, P., Rafkin, S. C., and Chattopadhyay, G. (2018). Retrieval of wind, temperature, water vapor and other trace constituents in the martian atmosphere. *Planetary and Space Science*, 161:26–40. https://doi.org/10.1016/j.pss.2018.05.004.

[Smith, 2002] Smith, M. D. (2002). The annual cycle of water vapor on mars as observed by the thermal emission spectrometer. *Journal of Geophysical Research: Planets*, 107(E11):25–1–25–19. https://doi.org/10.1029/2001je001522.

[Steele et al., 2014] Steele, L. J., Lewis, S. R., Patel, M. R., Montmessin, F., Forget, F., and Smith, M. D. (2014). The seasonal cycle of water vapour on mars from assimilation of thermal emission spectrometer data. *Icarus*, 237:97–115. https://doi.org/10.1016/j.icarus.2014.04.017.

[Virtanen et al., 2020] Virtanen, P., Gommers, R., Oliphant, T. E., Haberland, M., Reddy, T., Cournapeau, D., Burovski, E., Peterson, P., Weckesser, W., Bright, J., van der Walt, S. J., Brett, M., Wilson, J., Jarrod Millman, K., Mayorov, N., Nelson, A. R. J., Jones, E., Kern, R., Larson, E., Carey, C., Polat, İ., Feng, Y., Moore, E. W., Vand erPlas, J., Laxalde, D., Perktold, J., Cimrman, R., Henriksen, I., Quintero, E. A., Harris, C. R., Archibald, A. M., Ribeiro, A. H., Pedregosa, F., van Mulbregt, P., and Contributors (2020). SciPy 1.0: Fundamental Algorithms for Scientific Computing in Python. *Nature Methods*, 17:261–272.